

Thermally driven quantum refrigerator autonomously resets superconducting qubit

Mohammed Ali Aamir,^{1,*} Paul Jamet Suria,¹ José Antonio Marín Guzmán,² Claudia Castillo-Moreno,¹ Jeffrey M. Epstein,^{2,3} Nicole Yunger Halpern,^{2,3,†} and Simone Gasparinetti^{1,‡}

¹*Department of Microtechnology and Nanoscience,
Chalmers University of Technology, 412 96 Gothenburg, Sweden*
²*Joint Center for Quantum Information and Computer Science,
NIST and University of Maryland, College Park, MD 20742, USA*

³*Institute for Physical Science and Technology, University of Maryland, College Park, MD 20742, USA*
(Dated: March 20, 2025)

Although classical thermal machines power industries and modern living, quantum thermal engines have yet to prove their utility. Here, we demonstrate a useful quantum absorption refrigerator formed from superconducting circuits. We use it to cool a transmon qubit to a temperature lower than that achievable with any one available bath, thereby resetting the qubit to an initial state suitable for quantum computing. The process is driven by a thermal gradient and is autonomous, requiring no external feedback. The refrigerator exploits an engineered three-body interaction between the target qubit and two auxiliary qudits. Each auxiliary qudit is coupled to a physical heat bath, realized with a microwave waveguide populated with synthesized quasithermal radiation. If the target qubit is initially fully excited, its effective temperature reaches a steady-state level of approximately 22 mK, lower than what can be achieved by existing state-of-the-art reset protocols. Our results demonstrate that superconducting circuits with propagating thermal fields can be used to experimentally explore quantum thermodynamics and apply it to quantum information-processing tasks.

Quantum thermodynamics should be more useful. The field has yielded fundamental insights, such as extensions of the second law of thermodynamics to small, coherent, and far-from-equilibrium systems [1–13]. Additionally, quantum phenomena have been shown to enhance engines [14–19], batteries [20], and refrigeration [21, 22]. These results are progressing gradually from theory to proof-of-principle experiments. However, quantum thermal technologies remain experimental curiosities, not practical everyday tools. Key challenges include control [23] and cooling quantum thermal machines to temperatures that support quantum phenomena. Both challenges require substantial energy and effort but yield small returns. For example, one would expect a single-atom engine to perform only about an electronvolt of work [24].

Autonomous quantum machines offer hope. First, they operate without external control. Second, they run on heat drawn from thermal baths, which are naturally abundant [25]. A quantum thermal machine would be useful in a context that met three criteria: (i) The machine fulfills a need. (ii) The machine can access real-world different-temperature baths. (iii) No or few extra resources are spent on maintaining whatever coherence is necessary for the machine’s operation.

We identify such a context: qubit reset. Consider a superconducting quantum computer starting a calculation. The computer requires qubits initialized to their ground states [26]. If left to thermalize with its environment

as thoroughly as possible, though, a qubit could achieve only an excited-state population of ≈ 0.01 to 0.03 , or an effective temperature of 45 mK to 70 mK [27–30]. Furthermore, such passive thermalization takes a few multiples of the qubit’s energy-relaxation time—hundreds of microseconds in state-of-the-art setups—delaying the next computation. A quantum machine cooling the qubits to their ground (minimal-entropy) states fulfills criterion (i). Moreover, superconducting qubits inhabit a dilution refrigerator formed from nested plates, whose temperatures decrease from the outermost plate to the innermost. These temperature plates can serve as heat baths, meeting criterion (ii). Finally, the machine can retain its quantum nature if mounted on the coldest plate, next to the quantum processing unit, satisfying criterion (iii). Such an autonomous machine would be a *quantum absorption refrigerator*.

Quantum absorption refrigerators have been widely studied theoretically [31–51]. Reference [52] reported a landmark proof-of-principle experiment performed with trapped ions. However, the heat baths were emulated with electric fields and lasers, rather than realized with physical heat reservoirs. Other quantum refrigerators, motivated by possible applications, have been proposed [53, 54] and tested [55–57] but are not autonomous.

We report on a quantum absorption refrigerator realized with superconducting circuits. Our quantum refrigerator cools—and therefore resets—a target superconducting qubit *autonomously*. The target qubit’s energy-relaxation time is fully determined by the temperature of a hot bath we can vary. Using this control, we can vary the energy-relaxation time by a factor of > 70 . The reset’s fidelity is competitive: The target’s excited-state population reaches below $3 \times 10^{-4} \pm 2 \times 10^{-4}$

* aamir.ali@chalmers.se

† nicoleyh@umd.edu

‡ simoneg@chalmers.se

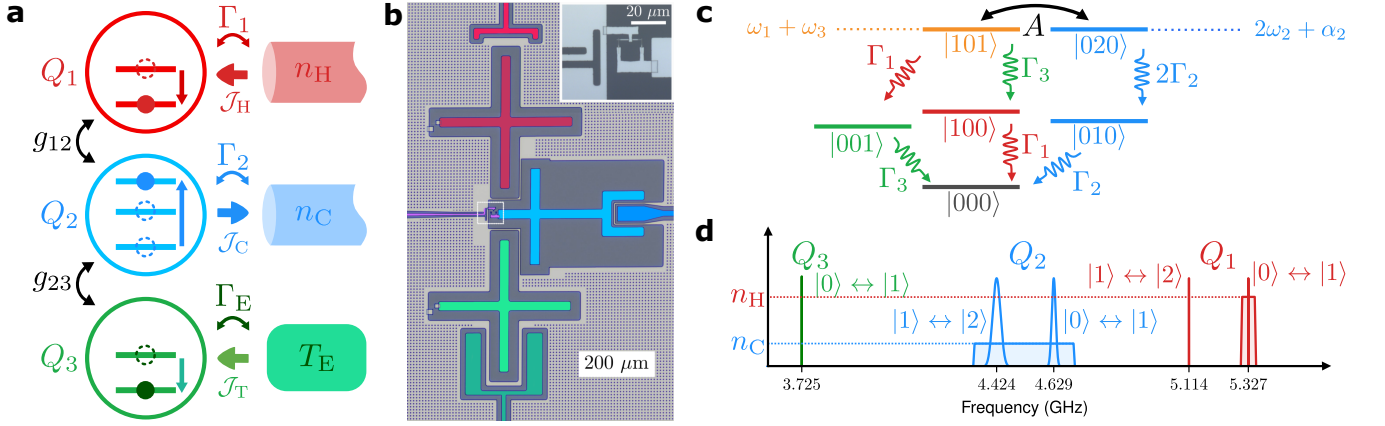


FIG. 1: Quantum-absorption-refrigerator scheme and level diagram. **a**, Conceptual scheme with three qudits. Qubit Q_1 couples directly to a waveguide at a rate Γ_1 ; and qudit Q_2 , to another waveguide at a rate Γ_2 . Qubit Q_3 couples undesirably to an uncontrolled bath in its environment. This bath keeps Q_3 at an effective temperature T_E . The coupling rate Γ_{relax} determines Q_3 's natural energy-relaxation time. The waveguides can operate as heat baths containing photons of average numbers n_H and n_C . The interqudit couplings (g_{12} , g_{23}) engender a process in which one excitation in Q_1 and one excitation in Q_3 are simultaneously exchanged with a double excitation in Q_2 . This exchange helps reset Q_3 . When heat baths drive this process, the system operates as an autonomous quantum refrigerator. The average heat currents are depicted by wide arrows from the hot (\mathcal{J}_H), cold (\mathcal{J}_C), and target (\mathcal{J}_T) systems' baths. By energy conservation, $\mathcal{J}_H + \mathcal{J}_T = \mathcal{J}_C$. **b**, False-color micrograph of the device implemented with superconducting circuits. Q_2 is frequency-tunable, due to a flux current line and two parallel Josephson junctions, magnified in the inset. **c**, Level diagram showing tensor products $|q_1q_2q_3\rangle$ of the qudits' energy eigenstates. $|101\rangle$ and $|020\rangle$ are resonant if $\omega_1 + \omega_3 = 2\omega_2 + \alpha_2$. At resonance, a three-body interaction couples the states at a rate A . **d**, Distributions over the qudits' experimentally observed transition frequencies. The Lorentzian distributions' widths represent spectral widths. The red shaded box depicts the spectral density n_H of photons injected into the waveguide coupled to Q_1 . This synthesized noise realizes the refrigerator's hot thermal bath. Analogous statements concern the blue box, n_C , Q_2 , and the cold bath.

[effective temperatures as low as 22 (+2, -3) mK]. In comparison, state-of-the-art reset protocols achieve populations of 8×10^{-4} to 2×10^{-3} (effective temperatures of 40 mK to 49 mK) [29, 30]. Our experiment demonstrates that quantum thermal machines not only can be useful, but also can be integrated with quantum information-processing units. Furthermore, such a practical autonomous quantum machine costs less control and thermodynamic work than its nonautonomous counterparts [58–60].

Our absorption refrigerator consists of three qudits (d -level quantum systems), as depicted in Fig. 1a. The auxiliary qudits Q_1 and Q_2 correspond to $d = 2, 3$, respectively. Each of them couples directly to a waveguide that supports a continuum of electromagnetic modes. The waveguide can serve as a heat bath formed from photons of an arbitrary spectral profile. n_H and n_C denote the average numbers of photons in the waveguides. The target of the refrigerator's cooling is qubit Q_3 , which is undesirably coupled to an uncontrolled bath in its environment. This bath excites the target to an effective temperature T_E . Nearest-neighbor qudits couple together with strengths g_{12} and g_{23} . These couplings result in an effective three-body interaction [61], a crucial ingredient in a quantum absorption refrigerator [25, 32, 33, 38]. We engineer the three-body interaction such that one excitation in Q_1 and one excitation in Q_3 are simultaneously, coherently exchanged with a double excitation in Q_2 . Losing

its excitation, Q_3 is reset.

As the heat baths drive the resetting, the system operates autonomously as a quantum absorption refrigerator [44]. A generic thermodynamic model describes such a refrigerator as follows. Heat flows from a hot bath (coupled to Q_1) into an intermediate-temperature bath (coupled to Q_2). A heat current \mathcal{J}_H (\mathcal{J}_T) flows out of Q_1 's (Q_3 's) bath. A net heat current $\mathcal{J}_C = \mathcal{J}_H + \mathcal{J}_T$ enters Q_2 's bath (Fig. 1a). That is, a temperature gradient, rather than work, coaxes heat out of the target qubit.

The qudits are Al-based superconducting transmons that have Al/AlO_x/Al Josephson junctions [62]. We arrange the qudits spatially in a linear configuration (Fig. 1b). The capacitances between the transmons couple the qudits mutually. Qudit Q_1 has a transition frequency $\omega_1/(2\pi) = 5.327$ GHz; and qudit Q_2 , a variable frequency $\omega_2/(2\pi)$. Q_1 couples capacitively to a microwave waveguide directly, at a dissipation rate $\Gamma_1/(2\pi) = 70$ kHz; and Q_2 couples to another waveguide at $\Gamma_2/(2\pi) = 7.2$ MHz. The third qubit, Q_3 , has a transition frequency $\omega_3/(2\pi) = 3.725$ GHz. Q_3 couples dispersively to a coplanar waveguide resonator. Via the resonator, we read out Q_3 's state and drive Q_3 coherently. In addition, Q_3 couples to the uncontrolled bath in its environment at a rate Γ_E . In our proof-of-concept demonstration, Q_3 stands in for a computational qubit that is being reset and that may participate in a larger processing unit. In the present design, Q_3 has a natural

energy-relaxation time $T_{\text{relax}} = 1/\Gamma_E = 16.8 \mu\text{s}$, limited largely by Purcell decay into the nearest waveguide, and a residual excited-state population $P_{\text{res}} = 0.028$. In future realizations, one can increase T_{relax} using Purcell filters [63].

The interqudit couplings hybridize the qudit modes. The hybridization, together with the Josephson junctions' nonlinearity, results in a three-body interaction (Supplementary Information). For this interaction to be resonant, the qudit frequencies must meet the condition $\omega_1 + \omega_3 = 2\omega_2^{\text{res}} + \alpha_2$. Here, ω_2^{res} denotes the Q_2 frequency that satisfies the equality, and α_2 denotes Q_2 's anharmonicity. The interaction arises from a four-wave mixing process: One excitation in Q_1 and one excitation in Q_3 are simultaneously exchanged with a double excitation in Q_2 (Fig. 1a) [61]. To satisfy the resonance condition *in situ*, we make Q_2 frequency-tunable [62]. We control the frequency with a magnetic flux induced by a nearby current line. The device is mounted in a dilution refrigerator that reaches 10 mK.

To describe the resonance condition, we introduce further notation. Let $|0\rangle$ and $|1\rangle$ denote the ground and first-excited states of any qudit. Let $|2\rangle$ denote the second-excited state of Q_2 . We represent a three-qudit state by $|q_1 q_2 q_3\rangle := |q_1\rangle_1 \otimes |q_2\rangle_2 \otimes |q_3\rangle_3$. The resonance condition leads to coherence between the states $|101\rangle$ and $|020\rangle$. This coherence is a key quantum feature of our refrigerator. Two processes, operating in conjunction, reset Q_3 : (i) Levels $|101\rangle$ and $|020\rangle$ coherently couple with an effective strength A (Fig. 1c). (ii) Q_2 dissipates into its waveguide at a rate Γ_2 . The combined action of (i) and (ii) brings $|101\rangle$ rapidly to $|010\rangle$ (and then to $|000\rangle$), thereby resetting Q_3 .

We engineer the heat baths of Q_1 and Q_2 as follows. First, we synthesize radiation using room-temperature electronics (Supplementary Figure S1). This radiation has a white-noise spectral profile over a selected frequency range. The radiation is injected into microwave coaxial cables, which are interlinked by dissipative microwave attenuators thermalized at different temperatures of the cryostat. The attenuators reduce the incoming radiation's power, while simultaneously introducing quantum thermal noise [64–66]. The last attenuator, at 10 mK, contributes noise that is predominantly quantum vacuum noise. This resulting radiation finally reaches Q_1 's and Q_2 's waveguides. Quantum noise is generally characterized by a non-symmetrical spectral density resulting in different emission and absorption rates of a qudit [67]. Here, the predominance of spontaneous emission of Q_2 into the cold bath (as opposed to absorption) is critical to the refrigerator's operation.

The bandwidth of the synthesized radiation is selected to include the frequencies of Q_1 's transitions ($|0\rangle \leftrightarrow |1\rangle$) and Q_2 's transitions ($|0\rangle \leftrightarrow |1\rangle$ and $|1\rangle \leftrightarrow |2\rangle$) (Fig. 1d). Within this bandwidth, the radiation can be approximated as a thermal field. Outside the bandwidth, however, the radiation deviates from thermality. Therefore, we designate this field as *quasithermal*. Its effective

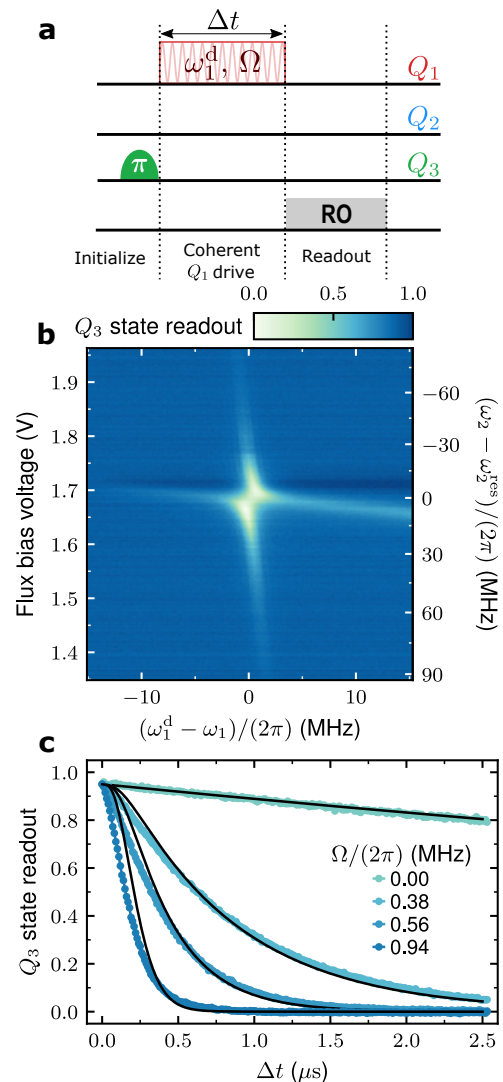


FIG. 2: Three-body interaction: **a**, Pulse scheme (see the main text for description). **b**, 2D plot of Q_3 's excited-state population ($[(\sigma_z) + \mathbb{1}]/2$), as a function of (i) the flux current (left axis) modulating Q_2 's frequency and (ii) the detuning between the Q_1 -drive frequency $\omega_1^d/(2\pi)$ and $\omega_1/(2\pi)$ (bottom axis). Q_1 is driven for $\Delta t = 2 \mu\text{s}$ during the pulse scheme, after which we read out (RO) Q_3 's state via the resonator. The left axis translates directly into the right axis—the detuning of the Q_2 frequency, $\omega_2/(2\pi)$, from the resonant value, $\omega_2^{\text{res}}/(2\pi)$. The white patch evidences an avoided crossing, where $|101\rangle$ and $|020\rangle$ become resonant (Fig. 1c). **c**, Excited-state readout of Q_3 as a function of the duration Δt of the Q_1 drive, at select drive rates $\Omega/(2\pi)$. The solid black lines are fits based on the model shown in Supplementary Section II.

temperature, $T_{\text{H,C}}$, depends on the average number of photons at the qudit $Q_{1,2}$ transition frequency: $n_{\text{H,C}} = 1/[\exp(\hbar\omega_{1,2}/k_{\text{B}}T_{\text{H,C}}) - 1]$. k_{B} is Boltzmann's constant. We can vary $n_{\text{H,C}}$ by regulating the synthesized noise's power. This setup enables the whole system to function as a quantum thermal machine. The quasither-

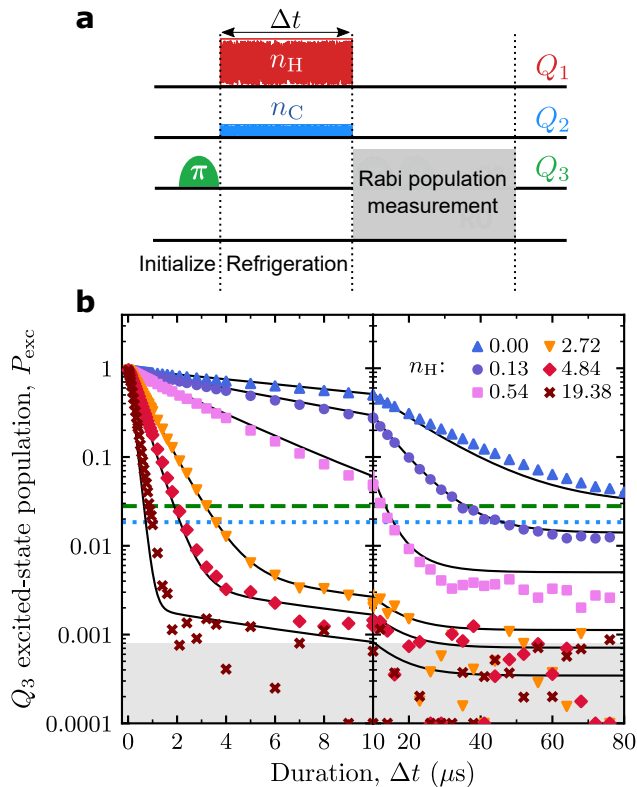


FIG. 3: Autonomous refrigeration enabled by a hot bath. **a**, Three-step pulse scheme: Initialization brings Q_3 's state close to $|1\rangle$. During refrigeration, Q_1 and Q_2 interact with synthesized quasithermal fields for a duration Δt . Finally, Q_3 's excited-state population, P_{exc} , is measured via a Rabi population-measurement scheme. P_{exc} represents combined populations of the first and second excited states; the latter is calculated based on a fitted theoretical model and is negligible except at intermediate values of Δt (Supplementary Section III). **b**, P_{exc} as a function of Δt , at select values of n_H , the average number of photons in the hot bath. The x -axis is split into two *different* regimes of Δt values: a low regime $\Delta t \in [0, 10] \mu\text{s}$ and a high regime $\Delta t \in [10, 80] \mu\text{s}$. Q_2 experiences no synthesized quasithermal field. We estimate that $n_C \approx 0.007$ due to the residual thermal field. The dashed green line shows Q_3 's residual excited-state population (defined in the main text), $P_{\text{res}} = 0.028$. The dotted blue line shows the excited-state population that Q_3 would have at the cold bath's temperature (45 mK), $P_C = 0.020$. The gray area represents our estimate of the noise floor (Supplementary Section IV). Near the noise floor, some measurements yield small negative values, represented by data points at the bottom axis. Solid lines represent global fits to the experimental curves. The fits are calculated from the model shown in Supplementary Section II. n_H is the sole free-fitting parameter.

mal baths induce transitions in Q_1 and Q_2 , autonomously driving the reset via the three-body interaction.

Having specified the setup, we demonstrate the three-body interaction: We verify that Q_3 can be reset via resonant driving of Q_1 if and only if Q_2 meets the resonance condition. The qubits begin in $|000\rangle$, whereupon we issue

two microwave drive pulses (Fig. 2a). The first is a Gaussian π -pulse that excites Q_3 to state $|1\rangle$: $|000\rangle \rightarrow |001\rangle$.

The second pulse is flat and coherently drives Q_1 (effecting $|001\rangle \leftrightarrow |101\rangle$) at a frequency ω_1^d , with a rate Ω , for a duration Δt . Subsequently, we perform qubit-state readout on Q_3 (we measure $[\langle\sigma_z\rangle + 1]/2$) via Q_3 's resonator.

We investigate the readout's dependences on ω_1^d and on the flux bias voltage (proportional to flux current) that modulates the tunable Q_2 frequency. We have fixed $\Delta t = 2 \mu\text{s}$ and $\Omega/(2\pi) = 200 \text{ kHz}$. The microwave drives, we observe, deplete Q_3 's excited-state population (Fig. 2a). The depletion is the greatest when $\omega_2 = \omega_2^{\text{res}}$ and the drive is resonant ($\omega_1^d = \omega_1$)—when the resonant coupling A between $|101\rangle$ and $|020\rangle$ is the strongest.

The excited state of Q_3 is depleted by the cascaded processes $|001\rangle \leftrightarrow |101\rangle \leftrightarrow |020\rangle \rightarrow |010\rangle$. The combined effect of these processes resembles optical pumping—used to achieve population inversion in atomic physics—enabling qubit reset. Away from the resonance condition, the resonant coupling A decreases. Consequently, the excited-state population of Q_3 drops less as the $|101\rangle$ – $|020\rangle$ detuning grows.

Furthermore, we study the effect of increasing the driving rate Ω (Fig. 2c). When $\Omega = 0 \text{ MHz}$, Q_3 decays to its ground state (resets) at its natural energy-relaxation time ($16.8 \mu\text{s}$). As Ω increases, the reset happens increasingly quickly. By fitting a model based on a Lindblad master equation (Supplementary Section II), we determine that the three-body interaction has a strength of $A/(2\pi) = 3.2 \text{ MHz}$.

Having demonstrated the three-body interaction, we operate the three-qubit system as a quantum thermal machine. To measure the system's performance, we implement a three-step pulse sequence (Fig. 3a): (1) Excite Q_3 to near $|1\rangle$ (to an excited-state population of 0.95). (2) Fill the waveguides with quasithermal photons, as described above, for a variable time interval Δt . (3) Measure Q_3 's excited-state population (the first two excited states combined), using a Rabi population-measurement scheme [27, 28]. This scheme allows for a more accurate population measurement than standard qubit-state readout. This scheme functions optimally when Q_3 's second-excited-state population is negligible compared to the first-excited-state population. However, this condition may not always be met when the latter is extremely small ($\lesssim 0.004$). Nonetheless, we account for Q_3 's second-excited-state population, determined theoretically from a comprehensively fitted model, in all population measurements, which are recalibrated accordingly (Supplementary Section III). We assume that the second-excited-state population is exponentially suppressed, arising from the same uncontrolled bath causing the residual first-excited-state population. This recalibration is insignificant except in some narrow subsets of our experimental data, which lie outside the regime in which we evaluate our refrigerator's performance (see below).

We raise the effective temperature of the hot bath and

investigate how P_{exc} responds. To do so, we elevate the average number n_{H} of quasithermal photons in the hot bath by increasing the spectral power of the synthesized noise in Q_1 's waveguide. We perform this study in the absence of synthesized noise in the cold bath (coupled to Q_2), which contains the minimal average number n_{C} of photons. We infer the minimal n_{C} from an independent measurement, using Q_2 as a thermometer [66]: $n_{\text{C}} = 0.007$, associated with a temperature $T_{\text{C}} = 45$ mK. The greater the n_{H} value, the more quickly P_{exc} decays as we increase Δt (Fig. 3b). At the low value $n_{\text{H}} = 0.16$, P_{exc} drops below the residual excited-state population $P_{\text{res}} = 0.028$ (green dashed line in Fig. 3b), which Q_3 would achieve if left alone for a long time. We infer from this value that the effective temperature of Q_3 's environment bath $T_{\text{E}} = 50$ mK (see Fig. 1a). If thermalized at the cold bath's temperature (45 mK), Q_3 would have an excited-state population $P_{\text{C}} = 0.020$ (blue dotted line). If the hot bath is excited, P_{exc} reaches at least an order of magnitude lower than P_{res} and P_{C} . Our refrigeration scheme clearly outperforms passive thermalization with either the intrinsic bath of Q_3 or the coldest bath available. At $n_{\text{H}} = 19.38$ ($T_{\text{H}} = 5.1$ K), refrigeration reduces the effective energy-relaxation time of Q_3 , T_{relax} , from 16.8 μs to 230 ns. This reduction is by a factor of > 70 . Q_3 's population declines below 2×10^{-3} over 1.8 μs , before approaching a steady-state value below 0.0008, our measurement protocol's noise floor (Supplementary Section IV).

In an independent measurement, we study the steady-state population P_{SS} as a function of n_{H} or n_{C} , keeping the other quantity fixed (Fig. 4a). We define P_{SS} as the P_{exc} achieved after the duration $\Delta t = 105$ μs . This definition stems from the observation that, when the refrigerator is inactive ($n_{\text{H}} = 0.003$), Q_3 naturally relaxes to its steady-state residual population, P_{res} , by $\Delta t = 105$ μs . P_{SS} decreases rapidly as n_{H} increases. Furthermore, P_{SS} reaches its lowest values when n_{C} minimizes at 0.007, such that Q_2 is not excited. We overestimate the lowest reached P_{SS} and its error margin by computing the mean and standard deviation of all the measured P_{SS} values that lie below 0.0008, the noise floor (Supplementary Section IV shows the methodology). P_{SS} reaches a minimum $< 3 \times 10^{-4} \pm 2 \times 10^{-4}$, equivalent to a temperature $T_{\text{SS}} = 22$ (+2, -3) mK. This result is remarkably close to the prediction from a general theory of a quantum absorption refrigerator [44]: $T_{\text{SS}} = \frac{2\omega_2 + \alpha_2 - \omega_1}{(2\omega_2 + \alpha_2)/T_{\text{C}} - \omega_1/T_{\text{H}}} = 18.6$ mK, equivalent to $P_{\text{SS}} = 6.7 \times 10^{-5}$. In the limit as $n_{\text{H}} \rightarrow \infty$, T_{SS} decreases marginally to 18.5 mK. T_{SS} does not depend on the temperature T_{E} of the target's effective bath, if Γ_{E} is very small ($\ll 1/T_{\text{relax}}$), as in our system during refrigeration.

Also, raising the cold bath's temperature impedes the reset. Increasing n_{C} to 0.07—exciting Q_2 more—leads P_{SS} (as a function of n_{H}) to saturate at a higher value. Finally, consider fixing n_{H} and increasing n_{C} . P_{SS} increases rapidly, then saturates near 0.36. This saturation

occurs largely independently of n_{H} . The greater the n_{H} , though, the greater the initial (low- n_{C}) P_{SS} .

A standard figure of merit in the thermodynamic analysis of refrigerators is the coefficient of performance (COP) [38]. The COP is to refrigerators as efficiency is to heat engines. The steady-state COP is defined as $\mathcal{J}_{\text{T}}/\mathcal{J}_{\text{H}}$ (see Fig. 1a), that we numerically calculate from the theoretical model shown in Supplementary Section II. The steady-state COP is 0.7 when $T_{\text{H}} = 5.1$ K and $T_{\text{SS}} = 22$ mK. In terms of COP, our quantum refrigerator performs comparably to a macroscopic absorption refrigerator—namely, a common air conditioner (COP ≈ 0.7 [68]). In the quasistatic limit (as $\mathcal{J}_{\text{T}} \rightarrow 0$), the COP can reach its theoretical upper bound, the Carnot limit: $\frac{T_{\text{E}}(T_{\text{H}} - T_{\text{C}})}{T_{\text{H}}(T_{\text{C}} - T_{\text{E}})}$. Our quantum refrigerator has a Carnot bound of $0.95 > 0.7$, satisfying the second law of thermodynamics.

Another important performance metric is the time required to reset Q_3 . We define the reset time as the time required for P_{exc} to reach 0.01 (corresponding to 38.5 mK). The reset time reaches as low as 970 ns before rising slowly with n_{H} (Fig. 4b). We attribute the observed upturn to excessive dephasing of the coherent process $|101\rangle \leftrightarrow |020\rangle$, which is critical for refrigeration.

In summary, we have demonstrated the first quantum thermal machine being deployed to accomplish a useful task. The task—reset of a superconducting qubit—is crucial to quantum information processing. The machine—a quantum absorption refrigerator formed from superconducting circuits—cools and resets the target qubit to an excited-state population lower than that achieved with state-of-the-art active reset protocols, without requiring external control. Nevertheless, the refrigeration can be turned off when the target qubit serves in a computation: one can either change the hot bath's temperature or detune a qubit out of resonance, using an on-chip magnetic flux.

Our refrigerator has two main quantum features—discrete energy levels and a coherent exchange coupling between states $|101\rangle$ and $|020\rangle$. Another salient feature of our quantum thermal machine is its use of waveguides as physical heat baths. In contrast, other experiments have emulated heat baths [52, 59]. Our heat baths consist of quasithermal fields—syntheses of quantum thermal fields and finite-bandwidth artificial microwave noise. Our approach allows control over the baths' temperatures, the ability to tailor spectral properties of the heat baths, and the selection of the level transitions to be heated. Thus, this method can facilitate a rigorous study of quantum thermal machines. Our experimental setup can be modified to exploit real-world thermal baths, such as different-temperature plates of a dilution refrigerator. We have already demonstrated that our quantum refrigerator can reset a qubit effectively if it has access to a hot bath at a temperature of a few kelvin, without the need for tuning. Superconducting coaxial cables, together with infrared-blocking filters [69], can expose the qudits to thermal radiation emitted by hot resistors anchored to the suitable

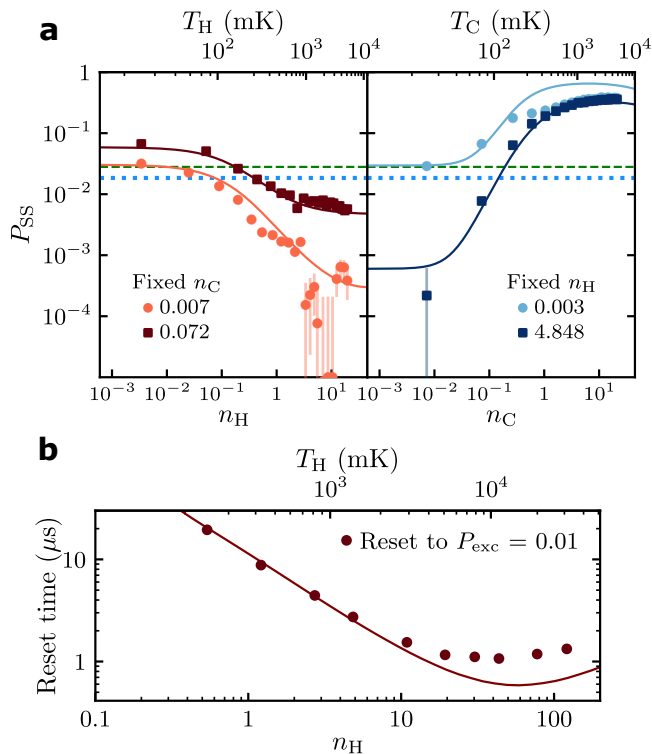


FIG. 4: Performance metrics of the quantum absorption refrigerator. **a**, After a $105 \mu\text{s}$ reset protocol, Q_3 's excited state reaches a steady-state excited-state population P_{SS} . (Left) P_{SS} as a function of the hot bath's average photon number, n_H . The corresponding temperature T_H is translated along the top axis. Two experimental curves are at two values of the cold bath's average photon number, n_C . (Right) P_{SS} as a function of n_C (translated into a temperature T_C on the top axis), at two n_H values. Some measurements yield small negative values, represented by data points at the bottom axis. The dashed green and dotted blue lines are the same as in Fig. 3b. **b**, Reset time (time required for Q_3 's P_{exc} to reach 0.01), as a function of n_H . All solid lines are theoretical predictions calculated from the model shown in Supplementary Section II.

dilution refrigerator's plate [70, 71]. The modification adds no significant heat load to the base-temperature plate; nor does it compromise the performance of the quantum information-processing unit. One can activate the thermal reset on demand in two different ways: (1) by using a microwave switch [72] to toggle Q_1 's bath between hot and cold or (2) by dynamically detuning Q_2 in and out of the resonance condition that enables the reset process.

Our quantum refrigerator initiates a path toward experimental studies of quantum thermodynamics with superconducting circuits coupled to propagating thermal microwave fields. Superconducting circuits may also offer an avenue toward scaling quantum thermal machines similarly to quantum-information processors. Our experiment may inspire the further development of useful, real-world applications of quantum thermodynamics [73]

to quantum information processing [74–76], thermometry [66, 71, 77], algorithmic cooling [55, 78], timekeeping [79], and entanglement generation [80]. This work marks a significant step in quantum thermodynamics toward practical applications.

REFERENCES

- [1] E. H. Lieb and J. Yngvason, The physics and mathematics of the second law of thermodynamics, *Physics Rep.* **310**, 1 (1999).
- [2] D. Janzing, P. Wocjan, R. Zeier, R. Geiss, and Th. Beth, Thermodynamic Cost of Reliability and Low Temperatures: Tightening Landauer's Principle and the Second Law, *Int. J. Th. Phys.* **39**, 2717 (2000).
- [3] D. Egloff, O. C. O. Dahlsten, R. Renner, and V. Vedral, A measure of majorization emerging from single-shot statistical mechanics, *New Journal of Physics* **17**, 073001 (2015).
- [4] M. Horodecki and J. Oppenheim, Fundamental limitations for quantum and nanoscale thermodynamics, *Nature communications* **4**, 2059 (2013).
- [5] F. Brandão, M. Horodecki, N. Ng, J. Oppenheim, and S. Wehner, The second laws of quantum thermodynamics, *Proceedings of the National Academy of Sciences* **112**, 3275 (2015).
- [6] N. Younger Halpern and J. M. Renes, Beyond heat baths: Generalized resource theories for small-scale thermodynamics, *Phys. Rev. E* **93**, 022126 (2016).
- [7] N. Y. Halpern, Beyond heat baths II: Framework for generalized thermodynamic resource theories, *J. Phys. A* **51**, 094001 (2018).
- [8] M. Lostaglio, D. Jennings, and T. Rudolph, Thermodynamic resource theories, non-commutativity and maximum entropy principles, *New J. Phys.* **19**, 043008 (2017).
- [9] Y. Guryanova, S. Popescu, A. J. Short, R. Silva, and P. Skrzypczyk, Thermodynamics of quantum systems with multiple conserved quantities, *Nature Comm.* **7**, 12049 (2016).
- [10] N. Younger Halpern, P. Faist, J. Oppenheim, and A. Winter, Microcanonical and resource-theoretic derivations of the thermal state of a quantum system with noncommuting charges, *Nature Comm.* **7**, 12051 (2016).
- [11] C. Sparaciari, J. Oppenheim, and T. Fritz, Resource theory for work and heat, *Phys. Rev. A* **96**, 052112 (2017).
- [12] G. Gour, D. Jennings, F. Buscemi, R. Duan, and I. Marvian, Quantum majorization and a complete set of entropic conditions for quantum thermodynamics, *Nature communications* **9**, 5352 (2018).
- [13] Z. B. Khalian, M. N. Bera, A. Riera, M. Lewenstein, and A. Winter, Resource Theory of Heat and Work with Non-commuting Charges, *Annales Henri Poincaré* **24**, 1725 (2023).
- [14] S. W. Kim, T. Sagawa, S. De Liberato, and M. Ueda, Quantum Szilard Engine, *Phys. Rev. Lett.* **106**, 070401 (2011).
- [15] D. Gelbwaser-Klimovsky, A. Bylinskii, D. Gangloff, R. Islam, A. Aspuru-Guzik, and V. Vuletic, Single-Atom Heat Machines Enabled by Energy Quantization, *Phys. Rev. Lett.* **120**, 170601 (2018).
- [16] N. M. Myers and S. Deffner, Bosons outperform fermions:

- The thermodynamic advantage of symmetry, *Phys. Rev. E* **101**, 012110 (2020).
- [17] M. Lostaglio, Certifying Quantum Signatures in Thermodynamics and Metrology via Contextuality of Quantum Linear Response, *Physical Review Letters* **125**, 230603 (2020).
- [18] A. A. S. Kalaei, A. Wacker, and P. P. Potts, Violating the thermodynamic uncertainty relation in the three-level maser, *Physical Review E* **104**, L012103 (2021).
- [19] K. Hammam, H. Leitch, Y. Hassouni, and G. De Chiara, Exploiting coherence for quantum thermodynamic advantage, *New Journal of Physics* **24**, 113053 (2022).
- [20] F. C. Binder, S. Vinjanampathy, K. Modi, and J. Goold, Quantacell: Powerful charging of quantum batteries, *New Journal of Physics* **17**, 075015 (2015).
- [21] D. Jennings and T. Rudolph, Entanglement and the thermodynamic arrow of time, *Phys. Rev. E* **81**, 061130 (2010).
- [22] A. Levy and M. Lostaglio, Quasiprobability Distribution for Heat Fluctuations in the Quantum Regime, *PRX Quantum* **1**, 010309 (2020).
- [23] M. P. Woods and M. Horodecki, Autonomous Quantum Devices: When Are They Realizable without Additional Thermodynamic Costs?, *Physical Review X* **13**, 011016 (2023).
- [24] J. Roßnagel, S. T. Dawkins, K. N. Tolazzi, O. Abah, E. Lutz, F. Schmidt-Kaler, and K. Singer, A single-atom heat engine, *Science* **352**, 325 (2016).
- [25] M. T. Mitchison, M. P. Woods, J. Prior, and M. Huber, Coherence-assisted single-shot cooling by quantum absorption refrigerators, *New Journal of Physics* **17**, 115013 (2015).
- [26] D. P. DiVincenzo, The Physical Implementation of Quantum Computation, *Fortschritte der Physik* **48**, 771 (2000).
- [27] K. Geerlings, Z. Leghtas, I. M. Pop, S. Shankar, L. Frunzio, R. J. Schoelkopf, M. Mirrahimi, and M. H. Devoret, Demonstrating a Driven Reset Protocol for a Superconducting Qubit, *Phys. Rev. Lett.* **110**, 120501 (2013).
- [28] X. Y. Jin, A. Kamal, A. P. Sears, T. Gudmundsen, D. Hover, J. Miloxi, R. Slattey, F. Yan, J. Yoder, T. P. Orlando, S. Gustavsson, and W. D. Oliver, Thermal and Residual Excited-State Population in a 3D Transmon Qubit, *Physical Review Letters* **114**, 240501 (2015).
- [29] P. Magnard, P. Kurpiers, B. Royer, T. Walter, J.-C. Besse, S. Gasparinetti, M. Pechal, J. Heinsoo, S. Storz, A. Blais, and A. Wallraff, Fast and Unconditional All-Microwave Reset of a Superconducting Qubit, *Phys. Rev. Lett.* **121**, 060502 (2018).
- [30] Y. Zhou, Z. Zhang, Z. Yin, S. Huai, X. Gu, X. Xu, J. Allcock, F. Liu, G. Xi, Q. Yu, H. Zhang, M. Zhang, H. Li, X. Song, Z. Wang, D. Zheng, S. An, Y. Zheng, and S. Zhang, Rapid and Unconditional Parametric Reset Protocol for Tunable Superconducting Qubits, *Nature Communications* **12**, 5924 (2021).
- [31] J. P. Palao, R. Kosloff, and J. M. Gordon, Quantum thermodynamic cooling cycle, *Physical Review E* **64**, 056130 (2001).
- [32] N. Linden, S. Popescu, and P. Skrzypczyk, How Small Can Thermal Machines Be? The Smallest Possible Refrigerator, *Physical Review Letters* **105**, 130401 (2010).
- [33] A. Levy and R. Kosloff, Quantum Absorption Refrigerator, *Physical Review Letters* **108**, 070604 (2012).
- [34] Y.-X. Chen and S.-W. Li, Quantum refrigerator driven by current noise, *EPL (Europhysics Letters)* **97**, 40003 (2012).
- [35] D. Venturelli, R. Fazio, and V. Giovannetti, Minimal Self-Contained Quantum Refrigeration Machine Based on Four Quantum Dots, *Phys. Rev. Lett.* **110**, 256801 (2013).
- [36] L. A. Correa, J. P. Palao, D. Alonso, and G. Adesso, Quantum-enhanced absorption refrigerators, *Sci. Rep.* **4**, 3949 (2014).
- [37] R. Silva, P. Skrzypczyk, and N. Brunner, Small quantum absorption refrigerator with reversed couplings, *Phys. Rev. E* **92**, 012136 (2015).
- [38] P. P. Hofer, M. Perarnau-Llobet, J. B. Brask, R. Silva, M. Huber, and N. Brunner, Autonomous quantum refrigerator in a circuit QED architecture based on a Josephson junction, *Phys. Rev. B* **94**, 235420 (2016).
- [39] A. Mu, B. K. Agarwalla, G. Schaller, and D. Segal, Qubit absorption refrigerator at strong coupling, *New Journal of Physics* **19**, 123034 (2017).
- [40] S. Nimmrichter, J. Dai, A. Roulet, and V. Scarani, Quantum and classical dynamics of a three-mode absorption refrigerator, *Quantum* **1**, 37 (2017).
- [41] J.-Y. Du and F.-L. Zhang, Nonequilibrium quantum absorption refrigerator, *New Journal of Physics* **20**, 063005 (2018).
- [42] V. Holubeč and T. Novotný, Effects of noise-induced coherence on the fluctuations of current in quantum absorption refrigerators, *The Journal of Chemical Physics* **151**, 044108 (2019).
- [43] M. T. Mitchison and P. P. Potts, Physical Implementations of Quantum Absorption Refrigerators, in *Thermodynamics in the Quantum Regime: Fundamental Aspects and New Directions*, Fundamental Theories of Physics, edited by F. Binder, L. A. Correa, C. Gogolin, J. Anders, and G. Adesso (Springer International Publishing, Cham, 2018) pp. 149–174.
- [44] M. T. Mitchison, Quantum thermal absorption machines: Refrigerators, engines and clocks, *Contemporary Physics* **60**, 164 (2019).
- [45] M. T. Naseem, A. Misra, and Ö. E. Müstecaplıoğlu, Two-body quantum absorption refrigerators with optomechanical-like interactions, *Quantum Science and Technology* **5**, 035006 (2020).
- [46] S. K. Manikandan, É. Jussiau, and A. N. Jordan, Autonomous quantum absorption refrigerators, *Physical Review B* **102**, 235427 (2020).
- [47] P. Arrangoiz-Arriola, E. A. Wollack, M. Pechal, J. D. Witmer, J. T. Hill, and A. H. Safavi-Naeini, Coupling a Superconducting Quantum Circuit to a Phononic Crystal Defect Cavity, *Phys. Rev. X* **8**, 031007 (2018).
- [48] B. Bhandari and A. N. Jordan, Minimal two-body quantum absorption refrigerator, *Phys. Rev. B* **104**, 075442 (2021).
- [49] M. Kloc, K. Meier, K. Hadjikyriakos, and G. Schaller, Superradiant Many-Qubit Absorption Refrigerator, *Phys. Rev. Applied* **16**, 044061 (2021).
- [50] M. W. AlMasri and M. R. B. Wahiddin, Bargmann Representation of Quantum Absorption Refrigerators, *Reports on Mathematical Physics* **89**, 185 (2022).
- [51] H. Okane, S. Kamimura, S. Kukita, Y. Kondo, and Y. Matsuzaki, *Quantum Thermodynamics applied for Quantum Refrigerators cooling down a qubit* (2022).
- [52] G. Maslennikov, S. Ding, R. Hablützel, J. Gan,

- A. Roulet, S. Nimmrichter, J. Dai, V. Scarani, and D. Matsukevich, Quantum absorption refrigerator with trapped ions, *Nature Communications* **10**, 202 (2019).
- [53] S. K. Manikandan and S. Qvarfort, Optimal quantum parametric feedback cooling, *Physical Review A* **107**, 023516 (2023).
- [54] T. Karmakar, É. Jussiau, S. K. Manikandan, and A. N. Jordan, Cyclic Superconducting Quantum Refrigerators Using Guided Fluxon Propagation, arXiv:2212.00277 [10.48550/arxiv.2212.00277](https://arxiv.org/abs/2212.00277) (2022).
- [55] J. Baugh, O. Moussa, C. A. Ryan, A. Nayak, and R. Laflamme, Experimental implementation of heat-bath algorithmic cooling using solid-state nuclear magnetic resonance, *Nature* **438**, 470 (2005).
- [56] A. Solfanelli, A. Santini, and M. Campisi, Quantum thermodynamic methods to purify a qubit on a quantum processing unit, *AVS Quantum Science* **4**, 026802 (2022).
- [57] L. Buffoni and M. Campisi, Cooperative quantum information erasure, *Quantum* **7**, 961 (2023).
- [58] A. Ronzani, B. Karimi, J. Senior, Y. Chang, J. T. Peltonen, C. Chen, and J. P. Pekola, Tunable photonic heat transport in a quantum heat valve, *Nature Physics* **14**, 991 (2018).
- [59] J. Klatzow, J. N. Becker, P. M. Ledingham, C. Weinzetl, K. T. Kaczmarek, D. J. Saunders, J. Nunn, I. A. Walmsley, R. Uzdin, and E. Poem, Experimental Demonstration of Quantum Effects in the Operation of Microscopic Heat Engines, *Phys. Rev. Lett.* **122**, 110601 (2019).
- [60] K. Y. Tan, M. Partanen, R. E. Lake, J. Govenius, S. Masuda, and M. Möttönen, Quantum-circuit refrigerator, *Nature Communications* **8**, 15189 (2017).
- [61] W. Ren, W. Liu, C. Song, H. Li, Q. Guo, Z. Wang, D. Zheng, G. S. Agarwal, M. O. Scully, S.-Y. Zhu, H. Wang, and D.-W. Wang, Simultaneous Excitation of Two Noninteracting Atoms with Time-Frequency Correlated Photon Pairs in a Superconducting Circuit, *Physical Review Letters* **125**, 133601 (2020).
- [62] J. Koch, T. M. Yu, J. Gambetta, A. A. Houck, D. I. Schuster, J. Majer, A. Blais, M. H. Devoret, S. M. Girvin, and R. J. Schoelkopf, Charge-insensitive qubit design derived from the Cooper pair box, *Phys. Rev. A* **76**, 042319 (2007).
- [63] M. D. Reed, B. R. Johnson, A. A. Houck, L. DiCarlo, J. M. Chow, D. I. Schuster, L. Frunzio, and R. J. Schoelkopf, Fast reset and suppressing spontaneous emission of a superconducting qubit, *Applied Physics Letters* **96**, 203110 (2010).
- [64] C. M. Caves, Quantum limits on noise in linear amplifiers, *Phys. Rev. D* **26**, 1817 (1982).
- [65] J. M. Fink, L. Steffen, P. Studer, L. S. Bishop, M. Baur, R. Bianchetti, D. Bozyigit, C. Lang, S. Filipp, P. J. Leek, and A. Wallraff, Quantum-To-Classical Transition in Cavity Quantum Electrodynamics, *Phys. Rev. Lett.* **105**, 163601 (2010).
- [66] M. Scigliuzzo, A. Bengtsson, J.-C. Besse, A. Wallraff, P. Delsing, and S. Gasparinetti, Primary Thermometry of Propagating Microwaves in the Quantum Regime, *Physical Review X* **10**, 041054 (2020).
- [67] A. A. Clerk, M. H. Devoret, S. M. Girvin, F. Marquardt, and R. J. Schoelkopf, Introduction to quantum noise, measurement, and amplification, *Rev. Mod. Phys.* **82**, 1155 (2010).
- [68] Module 10: Absorption refrigeration, CIBSE Journal <https://www.cibsejournal.com/cpd/modules/2009-11/> (2009).
- [69] R. Rehammar and S. Gasparinetti, Low-Pass Filter With Ultrawide Stopband for Quantum Computing Applications, *IEEE Transactions on Microwave Theory and Techniques* **10.1109/TMTT.2023.3238543** (2023).
- [70] J. Goetz, S. Pogorzalek, F. Deppe, K. G. Fedorov, P. Eder, M. Fischer, F. Wulschner, E. Xie, A. Marx, and R. Gross, Photon Statistics of Propagating Thermal Microwaves, *Phys. Rev. Lett.* **118**, 103602 (2017).
- [71] Z. Wang, M. Xu, X. Han, W. Fu, S. Puri, S. M. Girvin, H. X. Tang, S. Shankar, and M. H. Devoret, Quantum Microwave Radiometry with a Superconducting Qubit, *Physical Review Letters* **126**, 180501 (2021).
- [72] M. Pechal, J.-C. Besse, M. Mondal, M. Oppliger, S. Gasparinetti, and A. Wallraff, Superconducting Switch for Fast On-Chip Routing of Quantum Microwave Fields, *Phys. Rev. Applied* **6**, 024009 (2016).
- [73] J. A. M. Guzmán, P. Erker, S. Gasparinetti, M. Huber, and N. Y. Halpern, *Useful autonomous quantum machines* (2024), arXiv:2307.08739 [quant-ph].
- [74] M. Fellous-Asiani, J. H. Chai, R. S. Whitney, A. Auffèves, and H. K. Ng, Limitations in Quantum Computing from Resource Constraints, *PRX Quantum* **2**, 040335 (2021).
- [75] A. Auffèves, Quantum Technologies Need a Quantum Energy Initiative, *PRX Quantum* **3**, 020101 (2022).
- [76] M. Aifer and S. Deffner, From quantum speed limits to energy-efficient quantum gates, *New Journal of Physics* **24**, 055002 (2022).
- [77] M. Mehboudi, A. Sanpera, and L. A. Correa, Thermometry in the quantum regime: Recent theoretical progress, *Journal of Physics A: Mathematical and Theoretical* **52**, 303001 (2019).
- [78] Á. M. Alhambra, M. Lostaglio, and C. Perry, Heat-Bath Algorithmic Cooling with optimal thermalization strategies, *Quantum* **3**, 188 (2019).
- [79] P. Erker, M. T. Mitchison, R. Silva, M. P. Woods, N. Brunner, and M. Huber, Autonomous Quantum Clocks: Does Thermodynamics Limit Our Ability to Measure Time?, *Physical Review X* **7**, 031022 (2017).
- [80] J. B. Brask, G. Haack, N. Brunner, and M. Huber, Autonomous quantum thermal machine for generating steady-state entanglement, *New Journal of Physics* **17**, 113029 (2015).
- [81] S. E. Nigg, H. Paik, B. Vlastakis, G. Kirchmair, S. Shankar, L. Frunzio, M. H. Devoret, R. J. Schoelkopf, and S. M. Girvin, Black-Box Superconducting Circuit Quantization, *Phys. Rev. Lett.* **108**, 240502 (2012).
- [82] H. J. Carmichael and D. F. Walls, Master equation for strongly interacting systems, *Journal of Physics A: Mathematical, Nuclear and General* **6**, 1552 (1973).
- [83] A. Kulikov, R. Navarathna, and A. Fedorov, Measuring Effective Temperatures of Qubits Using Correlations, *Phys. Rev. Lett.* **124**, 240501 (2020).

Data availability: Supporting data are available in the figshare data repository (<https://doi.org/10.6084/m9.figshare.27089311.v1>).

ACKNOWLEDGMENTS

This work received support from the Swedish Research Council (M.A.A. and S.G.); the Knut and Alice Wal-

enberg Foundation through the Wallenberg Center for Quantum Technology (WACQT) (C.C.-M. and S.G.); the European Union, Quantum Flagship project ASPECTS (grant agreement number 101080167) (M.A.A.) and ERC ESQuAT (grant number 101041744) (S.G.); the National Science Foundation, under QLCI grant OMA-2120757 (N.Y.H.) and grant number NSF PHY-1748958 (J.M.E.); the John Templeton Foundation (award number 62422) (J.A.M.G.); and NIST grant number 70NANB21H055 (J.A.M.G.). The studied device was fabricated in Myfab Chalmers, a nanofabrication laboratory.

AUTHOR CONTRIBUTIONS

N.Y.H. and S.G. conceived the experiment. M.A.A., J.A.M.G., J.M.E., N.Y.H. and S.G. performed the theoretical modelling and designed the experiment. M.A.A., P.J.S. and S.G. designed the device. C.C.-M. fabricated the device. M.A.A., P.J.S. and S.G. performed the experiments. M.A.A. and S.G. analyzed and interpreted the results. M.A.A., N.Y.H. and S.G. wrote the manuscript with feedback from P.J.S. and J.A.M.G.

SUPPLEMENTARY INFORMATION

1. Full experimental setup and parameters

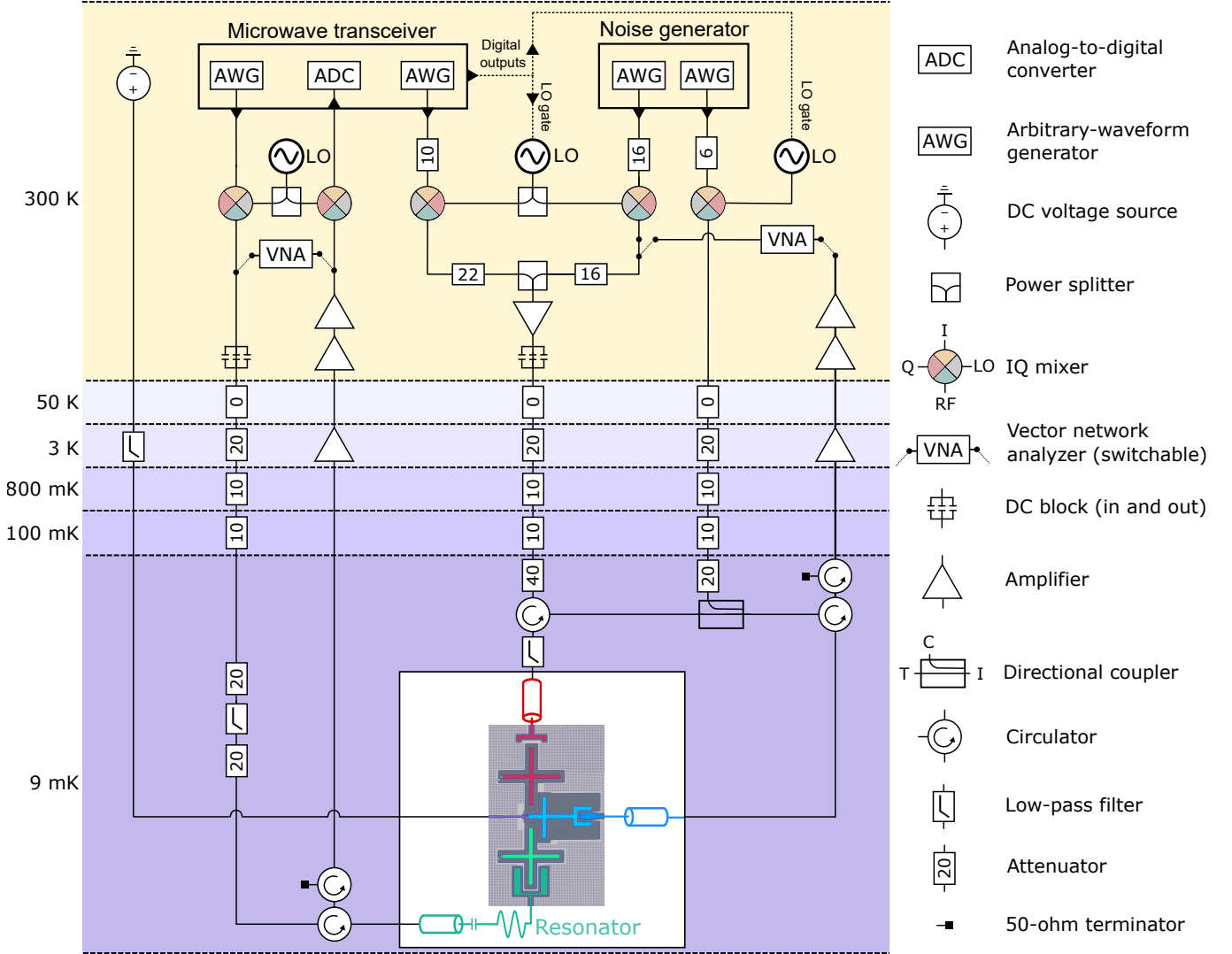


FIG. S1: Complete experimental set-up. See text for description. The in-phase-quadrature (IQ) mixers' ports, I and Q, are both used to connect to the microwave transceiver. However, only port I is shown to be wired; port Q is omitted for clarity. Digital outputs from the microwave transceiver are used to gate the local oscillators (LO) to produce pulses of thermal microwave modes. The directional coupler has 3 ports, called the input port (I), coupled port (C), and through port (T).

Figure S1 shows a schematic of the experimental set-up used to study our quantum absorption refrigerator (QAR). The QAR is packaged in a copper enclosure and mounted on the mixing-chamber stage of a dilution refrigerator that reaches 10 mK. The QAR is packaged in multiple layers: two nested copper enclosures shield the QAR from electromagnetic waves. A μ -metal enclosure protects the QAR from low-frequency magnetic fields. Microwave fields (both coherent and thermal) are routed to the QAR through highly attenuated input coaxial lines. The outgoing fields are routed through the output lines and are boosted by a cryogenic high-electron-mobility transistor (HEMT) amplifier (provided by Low Noise Factory) at 3 K and by room-temperature amplifiers. Microwave circulators separate the input and output signals. The resonator, dispersively coupled to qubit Q_3 , is probed by a microwave feedline in reflection mode. We probe and drive Q_1 and Q_2 , via the waveguide coupled to each, using two attenuated coaxial lines. We use a microwave directional coupler with three ports (input port, coupled port, and through port). Their arrangement allows us to use one output line for both Q_1 's and Q_2 's waveguides, taking advantage of the relevant transitions' nonoverlapping frequencies. Specifically, we combine the outgoing field from Q_1 (entering the through

Parameter	Symbol	Value
Q_1 mode frequency	$\omega_1/(2\pi)$	5.327 GHz
Q_2 mode-tunable frequency range	$\omega_2/(2\pi)$	4.2 GHz to 4.9 GHz
Q_2 resonant frequency	$\omega_2^{\text{res}}/(2\pi)$	4.629 GHz
Q_3 mode frequency	$\omega_3/(2\pi)$	3.725 GHz
Q_1 anharmonicity	$\alpha_1/(2\pi)$	-213.4 MHz
Q_2 anharmonicity	$\alpha_2/(2\pi)$	-205.1 MHz
Q_3 anharmonicity	$\alpha_3/(2\pi)$	-237.8 MHz
Q_1 radiative-emission rate	$\Gamma_1/(2\pi)$	70 kHz
Q_2 radiative-emission rate	$\Gamma_2/(2\pi)$	7.2 MHz
Q_3 natural energy-relaxation time	T_{relax}	16.8 μs
Three-body-coupling rate	$A/(2\pi)$	3.2 MHz

TABLE S1: Experimentally measured parameters' values.

port) with the incoming field (entering the coupled port) intended for Q_2 . The resultant field (exiting from the input port of the directional coupler) is routed by a circulator to Q_2 's waveguide.

We use a microwave transceiver (Vivace from Intermodulation Products, Sweden), with in-phase-quadrature (IQ) mixers and local oscillators (LO), for driving the qudits and for readout measurements of Q_3 . The physical connections can be switched to a vector network analyzer (VNA). The VNA is used for continuous-wave spectroscopy that allows for basic characterization, e.g., of a qudit's frequency and anharmonicity.

The waveguide coupled to Q_1 is populated with synthesized thermal microwave modes limited to a 50 MHz bandwidth centered at the qubit's frequency. An analogous statement concerns the waveguide coupled to Q_2 . To populate the waveguides, we first continuously generate voltage noise with a white (flat) spectral density, using an arbitrary-waveform generator (AWG) limited to a 50 MHz bandwidth centered at a frequency of 100 MHz. The equipment used is a Keysight 3202A, which is limited to a 500 MHz bandwidth. Next, the generated noise is up-converted with IQ mixers and microwave tones (≈ 4 GHz to 6 GHz) generated by an LO. Finally, the resulting continuous thermal radiation is chopped into pulses synchronized with Q_3 -state readouts (see Fig. 3 in the main text). This process is performed via modulation (gating) of the LO outputs (Anapico APMS20G-4-ULN), with help from the transceiver's digital logic outputs, over time intervals of 10 ns and longer. To characterize the qudits (e.g., to determine their frequencies), we can switch the input/output lines to VNA. Furthermore, to observe the three-body interactions with coherent drives (see Fig. 2 in the main text), we can switch qubit Q_1 's input line to the transceiver's AWG¹. Table S1 shows the QAR's experimentally inferred parameters.

2. Theoretical model

The Hamiltonian of our QAR's three-qudit system can be written as

$$\hat{H} = \sum_{i=1}^3 \left(\tilde{\omega}_i \hat{a}_i^\dagger \hat{a}_i + \alpha_i \hat{a}_i^\dagger \hat{a}_i^\dagger \hat{a}_i \hat{a}_i / 2 \right) + g_{12} \left(\hat{a}_1^\dagger \hat{a}_2 + \hat{a}_1 \hat{a}_2^\dagger \right) + g_{23} \left(\hat{a}_2^\dagger \hat{a}_3 + \hat{a}_2 \hat{a}_3^\dagger \right). \quad (\text{S1})$$

\hat{a}_i and \hat{a}_i^\dagger denote qudit Q_i 's annihilation and creation operators. $\tilde{\omega}_i$ and α_i denote qudit Q_i 's bare mode frequency and anharmonicity. g_{12} (g_{23}) denotes the rate of the coupling between qudits Q_1 and Q_2 (qudits Q_2 and Q_3).

We engineer an effective three-body interaction by meeting the resonance condition $\omega_1 + \omega_3 = 2\omega_2 + \alpha_2$ and using Josephson junctions that facilitate the four-wave mixing [61]. The three-body interaction interchanges the three-qudit states $|101\rangle$ and $|020\rangle$ (see the notation and Fig. 1c in the main text).

We now introduce an approximation to \hat{H} . Denote by A the rate at which $|101\rangle$ and $|020\rangle$ couple coherently. \hat{H} is

¹ Certain equipment, instruments, software, or materials are identified in this paper to specify the experimental procedure adequately. Such identification is not intended to imply the recom-

mendation or endorsement of any product or service by NIST; nor is it intended to imply that the materials or equipment identified are necessarily the best available for the purpose.

well-approximated by the effective Hamiltonian

$$\hat{H}_{\text{eff}} = \sum_{i=1}^3 \omega_i \hat{a}_i^\dagger \hat{a}_i + \sum_{i,j=1}^3 \frac{\alpha_{ij}}{2} \hat{a}_i^\dagger \hat{a}_i \hat{a}_j^\dagger \hat{a}_j + A (|101\rangle\langle 020| + |020\rangle\langle 101|). \quad (\text{S2})$$

The simplification follows from black-box quantization [81] and second-order time-independent perturbation theory [61]. H_{eff} depends on dressed modes associated with annihilation and creation operators \hat{a}_i and \hat{a}_i^\dagger , dressed-mode frequencies ω_i , and self-Kerr and cross-Kerr coupling rates α_{ij} .

Let us introduce into the model a drive, as shown in Fig. 2 of the main text. This coherent drive is applied to Q_1 at the drive frequency ω_d and the rate Ω . Upon adding a drive term to \hat{H}_{eff} , we apply the rotating-wave approximation. We obtain the full Hamiltonian

$$\hat{H}_{D1} = \sum_{i=1}^3 \delta_i \hat{a}_i^\dagger \hat{a}_i + \sum_{i,j=1}^3 \frac{\alpha_{ij}}{2} \hat{a}_i^\dagger \hat{a}_i \hat{a}_j^\dagger \hat{a}_j + A (|101\rangle\langle 020| + |020\rangle\langle 101|) + \frac{\Omega}{2} (\hat{a}_1 + \hat{a}_1^\dagger). \quad (\text{S3})$$

The effective frequency $\delta_i := \omega_d - \omega_i$.

To model the measurements of Fig. 2, we solve a Lindblad quantum master equation:

$$\frac{\partial \hat{\rho}}{\partial t} = -\frac{i}{\hbar} [\hat{H}_{D1}, \rho] + \sum_{i=1}^3 \Gamma_i \mathcal{D}[\hat{a}_i, \rho]. \quad (\text{S4})$$

We model the waveguides as zero-temperature baths (with average occupation numbers of 0). The qudits can interact with such baths just through spontaneous emission [82]. We have suppressed the time dependence of ρ in our notation. At all times t , ρ approximately equals the tensor product of the qudits' reduced states, ρ_i : $\rho = \rho_1 \otimes \rho_2 \otimes \rho_3$. $\Gamma_{i=1,2}$ denotes the rate at which qudit Q_i couples to its waveguide. Γ_E , Q_3 's natural energy-relaxation rate, is related to the qubit's energy-relaxation time T_{relax} when refrigerator is inactive through $\Gamma_E = 1/T_{\text{relax}}$. The dissipator superoperator \mathcal{D} is defined through

$$\mathcal{D}[\hat{A}, \hat{B}] = \hat{A} \hat{B} \hat{A}^\dagger - \frac{1}{2} (\hat{A}^\dagger \hat{A} \hat{B} + \hat{B} \hat{A}^\dagger \hat{A}), \quad (\text{S5})$$

for operators \hat{A} and \hat{B} .

To model the QAR interacting with two heat baths, we limit our analysis to a subspace of the full Hilbert space. This subspace is spanned by the basis $\mathcal{B} = \{|000\rangle, |100\rangle, |010\rangle, |001\rangle, |002\rangle, |102\rangle, |020\rangle, |101\rangle\}$ containing 8 levels.

The population of $|i\rangle \in \mathcal{B}$ is $p_i := \rho_{ii} := \langle i | \hat{\rho} | i \rangle$. We formulate an 8-level population-rate model to calculate these populations's dynamics. To capture the coherent exchanges between $|101\rangle$ and $|020\rangle$, we also include an off-diagonal element $\rho_{\text{coh}} = \langle 101 | \hat{\rho} | 020 \rangle$ in the model. Combining these ingredients, we introduce the rate equation for the populations:

$$\frac{d}{dt} \begin{pmatrix} p_{|000\rangle}(t) \\ p_{|100\rangle}(t) \\ p_{|010\rangle}(t) \\ p_{|001\rangle}(t) \\ p_{|002\rangle}(t) \\ p_{|102\rangle}(t) \\ p_{|020\rangle}(t) \\ p_{|101\rangle}(t) \\ \rho_{\text{coh}}(t) \end{pmatrix} = R_P \begin{pmatrix} p_{|000\rangle}(t) \\ p_{|100\rangle}(t) \\ p_{|010\rangle}(t) \\ p_{|001\rangle}(t) \\ p_{|002\rangle}(t) \\ p_{|102\rangle}(t) \\ p_{|020\rangle}(t) \\ p_{|101\rangle}(t) \\ \rho_{\text{coh}}(t) \end{pmatrix}. \quad (\text{S6})$$

The rate matrix R_P is defined as

$$R_P := \begin{pmatrix} -\Gamma_{1\uparrow} + \Gamma_{2\uparrow} + \Gamma_{3\uparrow} & \Gamma_{1\downarrow} & \Gamma_{2\downarrow} & \Gamma_{3\downarrow} & 0 & 0 & 0 & 0 & 0 \\ \Gamma_{1\uparrow} & -(\Gamma_{1\downarrow} + \Gamma_{3\uparrow}) & 0 & 0 & 0 & 0 & 0 & \Gamma_{3\downarrow} & 0 \\ \Gamma_{2\uparrow} & 0 & -(\Gamma_{2\downarrow} + 2\Gamma_{2\uparrow}) & 0 & 0 & 0 & 2\Gamma_{2\downarrow} & 0 & 0 \\ \Gamma_{3\uparrow} & 0 & 0 & -(\Gamma_{3\downarrow} + \Gamma_{1\uparrow} + 2\Gamma_{3f\uparrow}) & 2\Gamma_{3f\downarrow} & 0 & 0 & \Gamma_{1\downarrow} & 0 \\ 0 & 0 & 0 & 2\Gamma_{3f\uparrow} & -(\Gamma_{1\uparrow} + 2\Gamma_{3f\downarrow}) & \Gamma_{1\downarrow} & 0 & 0 & 0 \\ 0 & 0 & 0 & 0 & \Gamma_{1\uparrow} & -(\Gamma_{1\downarrow} + 2\Gamma_{3f\downarrow}) & 0 & 2\Gamma_{3f\uparrow} & 0 \\ 0 & 0 & 2\Gamma_{2\uparrow} & 0 & 0 & 0 & -2\Gamma_{2\downarrow} & 0 & 2A \\ 0 & \Gamma_{3\uparrow} & 0 & \Gamma_{1\uparrow} & 0 & 2\Gamma_{3f\downarrow} & 0 & -(\Gamma_{1\downarrow} + \Gamma_{3\downarrow} + 2\Gamma_{3f\uparrow}) & -2A \\ 0 & 0 & 0 & 0 & 0 & 0 & -A & A & \Gamma_C \end{pmatrix} \quad (S7)$$

We define the Γ 's as follows. Denote by n_i the average number of synthesized quasithermal photons in the waveguide coupled to qudit Q_i ; and, by $n_{i,\text{res}}$, the average number of native thermal (i.e., residual) photons already present in waveguide $i = 1, 2$. $n_{3,\text{res}}$ is the effective average number of photons that populate qudit Q_3 's environment and that affect Q_3 's *first transition*, $|000\rangle \leftrightarrow |001\rangle$. We also introduce $n_{3f,\text{res}}$ as the average number of photons affecting the Q_3 's *second transition*, $|001\rangle \leftrightarrow |002\rangle$. In terms of these quantities, we define lowering rates $\Gamma_{i\downarrow} = \Gamma_i(n_i + n_{i,\text{res}} + 1)$ and raising rates $\Gamma_{i\uparrow} = \Gamma_i(n_i + n_{i,\text{res}})$ for qudits $i \in \{1, 2\}$, as well as $\Gamma_{3\downarrow} = \Gamma_E(n_{3,\text{res}} + 1)$ and $\Gamma_{3\uparrow} = \Gamma_E n_{3,\text{res}}$. Similarly, $\Gamma_{3f\uparrow} = \Gamma_E n_{3f,\text{res}}$ and $\Gamma_{3f\downarrow} = \Gamma_E(n_{3f,\text{res}} + 1)$ denote the analogous rates at the frequency of Q_3 's second transition ($|001\rangle \leftrightarrow |002\rangle$). For brevity, Eq. (S7) also contains a new notation Γ_C defined as

$$\Gamma_C = -(2\Gamma_{2\downarrow} + 2\Gamma_{2\uparrow} + \Gamma_{1\downarrow} + \Gamma_{1\uparrow} + \Gamma_{3\downarrow} + \Gamma_{3\uparrow})/4.$$

To model the data in Figs. 3b, 4a and 4b, we solve Eq. (S6) with the initial condition

$$\begin{aligned} & (p_{|000\rangle}(0), p_{|100\rangle}(0), p_{|010\rangle}(0), p_{|001\rangle}(0), p_{|002\rangle}(0), p_{|102\rangle}(0), p_{|020\rangle}(0), p_{|101\rangle}(0), \rho_{\text{coh}}(0)) \\ & = (0.028, 0.003, 0.007, 1 - 0.028 - 0.0008, 0.0008, 0, 0, 0, 0). \end{aligned} \quad (S8)$$

This vector represents the state prepared before the refrigeration—the state that the system is in after the π -pulse that impacts Q_3 's 0–1 transition (see Fig. 3b in the main text). Before the π -pulse, the Q_3 states $|1\rangle$ and $|2\rangle$ contain residual populations of 0.028 (experimentally determined) and $0.028^2 = 0.0008$, respectively. We estimate Q_3 's $|2\rangle$ population under two assumptions: First, Q_3 's environment acts as a bath with the effective temperature T_E . This temperature is the same for both the transitions, $|0\rangle \leftrightarrow |1\rangle$ and $|1\rangle \leftrightarrow |2\rangle$. Second, Boltzmann factors determine the detailed-balance rate for both these transitions. Therefore, $P_1 = P_0 \exp[-\hbar\omega_3/(k_B T_E)]$, and $P_2 = P_1 \exp[-\hbar(\omega_3 + \alpha_3)/(k_B T_E)] = P_0 \exp[-\hbar(2\omega_3 + \alpha_3)/(k_B T_E)] \approx \{\exp[-\hbar\omega_3/(k_B T_E)]\}^2$. The last approximation is justified because $\alpha_3 \ll 2\omega_3$. Our assumption would have been undermined if two-level fluctuators were in Q_3 's environment, which could lead to widely different T_E across short frequency ranges [83]. However, we have observed that our measured P_{res} does not lie outside a fixed narrow range (see Sec. VII below) across thermal cyclings of the device. This observation supports our assumption that T_E is uniform across small frequency ranges. Thus, Q_3 's $|0\rangle$ level has a population $1 - 0.028 - 0.0008$. The populations of Q_1 's state $|1\rangle$ is 0.003. The populations of Q_2 's level $|1\rangle$ is 0.007. The aforementioned π -pulse exchanges the populations of the Q_3 levels $|0\rangle$ and $|1\rangle$, yielding the vector (S8).

Having introduced our dynamical model, we review the steady-state coefficient of performance (COP), following Ref. [38]. Denote by \mathcal{J}_T the steady-state current of heat drawn from the target system. Denote by \mathcal{J}_H the steady-state current of heat drawn by Q_1 from the hot bath. The currents' ratio equals an absorption refrigerator's steady-state COP:

$$\text{COP} := \mathcal{J}_T / \mathcal{J}_H. \quad (S9)$$

The steady-state heat current drawn from bath $i \in \{1, 2, 3\}$ is

$$\mathcal{J}_i = \text{Tr}(\hat{H}\mathcal{L}_i\rho(\infty)). \quad (S10)$$

The Lindbladian therein acts as $\mathcal{L}_i\hat{\rho} = \Gamma_i \left\{ (n_i + n_{i,\text{res}} + 1) \mathcal{D}[\hat{a}_i, \hat{\rho}] + (n_i + n_{i,\text{res}}) \mathcal{D}[\hat{a}_i^\dagger, \hat{\rho}] \right\}$.

3. Rabi population-measurement scheme

Figure S2 shows the pulse sequence used to measure Q_3 's level- $|1\rangle$ population more accurately than standard qubit readout allows [27, 28]. This Rabi scheme involves the Q_3 energy levels $|0\rangle$, $|1\rangle$, and $|2\rangle$. We measure the qubit-state readout in the subspace $\text{span}\{|1\rangle, |2\rangle\}$.

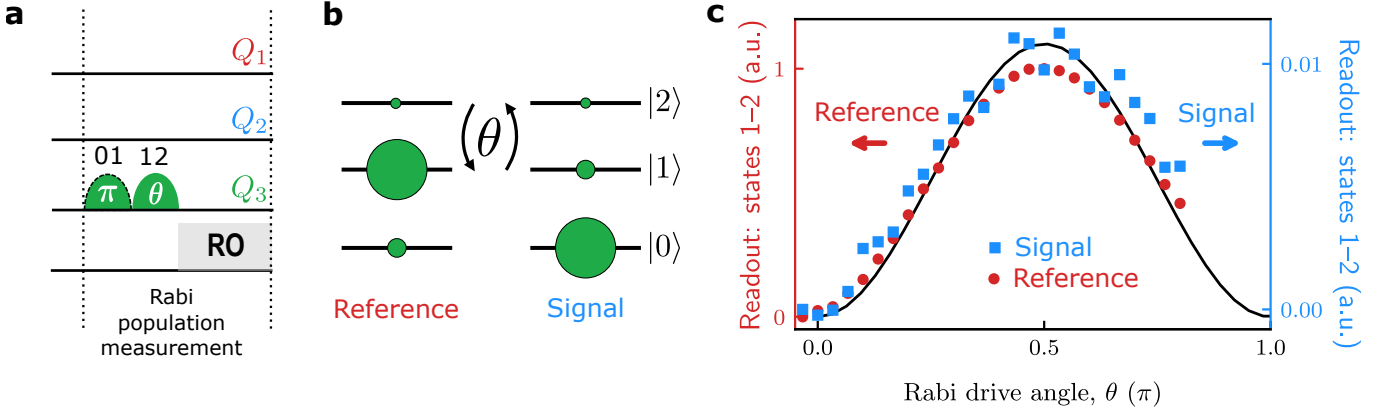


FIG. S2: Rabi measurement of the population in qubit Q_3 's $|1\rangle$ level. (a) Pulse sequence for the scheme. The notation 0–1 (1–2) indicates that the pulse drives the transition $|0\rangle \leftrightarrow |1\rangle$ ($|1\rangle \leftrightarrow |2\rangle$). θ denotes the pulse drive's Rabi angle. The pulse with the dashed outline is present in the reference measurement and absent from the signal measurement. The readout (RO) is performed in the subspace span $\{|1\rangle, |2\rangle\}$. (b) Representation of the relative distribution of populations across qubit Q_3 's $|0\rangle$, $|1\rangle$, and $|2\rangle$ levels when Q_3 is in its natural steady-state. (c) Rabi oscillations. The Rabi oscillation resulting from the 1–2 pulse after the 0–1 pulse provides a reference trace (red). The Rabi oscillation produced without the 1–2 pulse provides the signal—the actual population trace (blue).

The measured readout voltage can be expressed as

$$S = S_0P_0 + S_1P_1 + S_2P_2. \quad (\text{S11})$$

P_i denotes the population of Q_3 's i^{th} state, for $i \in \{0, 1, 2\}$. S_i represents the respective weighted coefficient. In the main text, we present the excited-state population, $P_1 + P_2$, as P_{exc} .

The scheme for measuring Q_3 's excited-state population involves two different Rabi oscillations. We drive Rabi oscillations between $|1\rangle$ and $|2\rangle$ in each of two cases: with and without a prior π -pulse in the subspace span $\{|0\rangle, |1\rangle\}$. The prior pulse interchanges the populations of $|0\rangle$ and $|1\rangle$, i.e., interchanges P_0 and P_1 (see the 0–1 pulse with the dashed outline in Fig. S2a). We measure and denote these Rabi oscillations' amplitudes by S_R (the Reference in Fig. S2c) and S_S (the Signal in Fig. S2c), respectively. We determine S_R and S_S , while saving experiment runtime as follows: We perform a two-point measurement at $\theta = 0$ and $\theta = \pi$, to determine the amplitudes of the Rabi oscillations. From those measurements, we compute a ratio S_P related to the populations P_1 and P_2 :

$$S_P = \frac{S_S}{S_S + S_R} = \frac{P_1 - P_2}{1 - 3P_2} \approx P_1 - P_2 \quad (\text{S12})$$

The last approximation holds if $P_2 \ll 1$.

Importantly, refrigeration with a large n_H results in a population P_1 that is very low ($\lesssim 0.001$) and is comparable to P_2 . Our scheme cannot separate these two populations' contributions to the measured S_P . Nonetheless, our quantitative 8-level model can yield a theoretical P_2 , which is multiplied by 2 and added to our measured S_P value. Thus, we obtain the excited-state population: $P_{\text{exc}} = P_1 + P_2$. The result agrees with the calculation (Fig. S3).

4. Population measurements near noise floor

Our population measurement is particularly challenging when the population reaches very low values—specifically below 0.001, which appears to be the noise floor of our population measurements in Fig. 3b. Given this experimental limitation, we interpret the data near this noise floor with special consideration and draw conservative conclusions. Our measurements near the noise floor also yield negative values sometimes, as reported in [28, 30]. The noise floor stems from the susceptibility of our measurement technique, which involves voltage-readout signals, to stochastic voltage noise in the measurement circuit—noise sourced predominantly by the circuit's amplifiers (see Fig. S1).

We make a conservative estimate of the noise floor of our population measurements, shown in the main text's Fig. 3b, as follows. We consider three representative datasets for which $n_H > 1$. We analyze fluctuations for values of time duration $\Delta t > 40 \mu\text{s}$. Here, our measurements appear close to or have reached the noise floor. Furthermore, the theoretical curves modelling the data relatively well, especially at low Δt , also indicate that the populations have

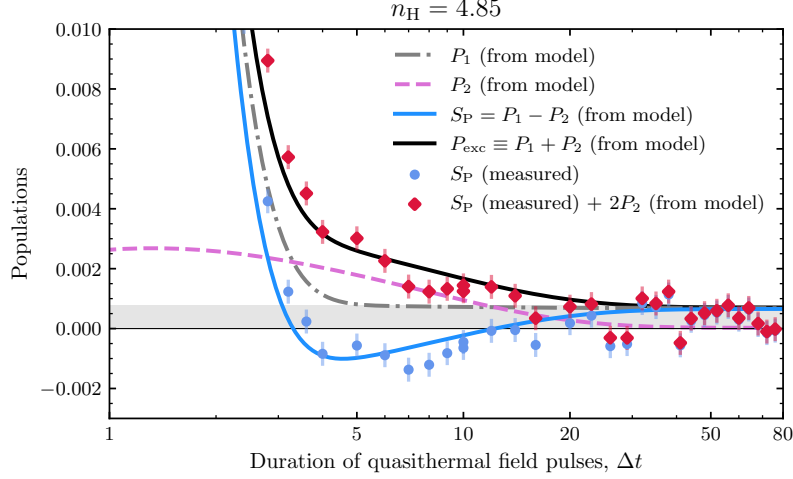


FIG. S3: Measured and calculated populations as functions of the time duration Δt of the applied quasithermal fields, with $n_H = 4.85$. This is one of the datasets presented in the main text's Fig. 3b. Recall that P_1 and P_2 denote the populations of Q_1 's $|1\rangle$ and $|2\rangle$ levels. These populations are calculated from the 8-level population-rate model in Eq. S6, presented in Sec. II. The experimentally inferred ratio S_P is related to the levels' populations as $P_1 - P_2$. The measured data (blue circles) is compared to the blue curve calculated theoretically. From the measured S_P and calculated P_2 , we obtain the excited-state population: $P_{\text{exc}} = S_P + 2P_2$ (cross-data points). This result is compared with the corresponding theoretical (black) curve, which represents $P_1 + P_2$. The error bars represent the standard deviations about the mean values, represented by symbols (see Sec. IV for method). The shaded area represents estimate of the measurement's noise floor (see Sec. IV for method). Accounting for P_2 is particularly important when P_{exc} reaches near 0.001 at intermediate Δt values, when P_1 may become comparable to P_2 . P_2 rises at intermediate Δt because of the population transfer from the Q_3 's state $|1\rangle$ to state $|2\rangle$ at rate $2\Gamma_{3fu}$ (see the rate equation in sec. II above). This process is impeded by the competing refrigeration process transferring population from state $|1\rangle$ to state $|0\rangle$ instead. At both low and high Δt values, P_2 is negligible compared to P_1 .

reached their steady-state values for $\Delta t > 40 \mu\text{s}$. We compute the standard deviation for each curve separately, for $\Delta t > 40 \mu\text{s}$, yielding three estimates of the uncertainty in our measurements. We regard their average as the uncertainty in our measurements, $\sigma = 0.0004$. We identify the noise floor as $2\sigma = 0.0008$ above zero; it is shaded in gray in Fig. 3b.

We perform a similar analysis to extract the value of, and uncertainty in, P_{SS} when it reaches its lowest value by refrigeration. Specifically, we analyze the experimental curve for P_{SS} as a function of n_H , at the lowest $n_C = 0.007$ (left plot of Fig. 4a). We acquired this dataset separately from the other three curves in Fig. 4a: We achieved a better signal-to-noise ratio (with more ensemble averaging and better qubit-readout settings), which is critical when P_{SS} is near the noise floor. We evaluate the lowest P_{SS} by computing the mean of the measured values of the curve that have declined below 0.0008 (an estimate of the noise floor identified above and depicted in Fig. 3b). This is a conservative evaluation of the mean. We are likely over-estimating the value of lowest P_{SS} , thereby underestimating our refrigerator's capability. We estimate the uncertainty by computing the standard deviation of the same set of values of P_{SS} . In conclusion, the mean and standard deviation are 3×10^{-4} and 2×10^{-4} , respectively. A similar procedure was applied for other experimental curves in Fig. 4a to determine the uncertainty. For those curves, the standard deviation is 5×10^{-4} .

5. Engineering guidelines

The main parameters usable to engineer our quantum refrigerator are the transition frequencies ω_1 , ω_2 , and ω_3 ; the dissipation rates Γ_1 and Γ_2 ; and the three-body-interaction strength A . The interaction exchanges $|101\rangle$ and $|020\rangle$ only when the transition frequencies satisfy the resonance condition,

$$\omega_1 + \omega_3 = 2\omega_2 + \alpha_2. \quad (\text{S13})$$

The greater the A , the more quickly our quantum refrigerator can cool the target qubit. In the perturbative

approximation (when $g_{12}, g_{23} \ll \omega_1, \omega_2, \omega_3$), A has the form [61]

$$A = \sqrt{2} g_{12} g_{23} \left(\frac{1}{2\omega_2 + \alpha_2 - \omega_1} + \frac{1}{2\omega_2 + \alpha_2 - \omega_3} \right). \quad (\text{S14})$$

$A/(2\pi)$ is limited to values on the order of few MHz, for the nominal parameter values of $g_{12}, g_{23}, \omega_1, \omega_2, \omega_3$, within the applicability of the full Hamiltonian's rotating-wave approximation. Our quantum refrigerator has two steady-state metrics: the target's steady-state temperature, T_{SS} , and the steady-state COP. We expect the generic quantum-absorption-refrigerator model [44] to describe our quantum refrigerator. It implies

$$T_{\text{SS}} = \frac{2\omega_2 + \alpha_2 - \omega_1}{(2\omega_2 + \alpha_2)/T_C - \omega_1/T_H}. \quad (\text{S15})$$

This result relies on the assumption that the target qubit couples to its environment only weakly (at a low rate Γ_E).

High T_H values (high n_H values) favor low T_{SS} values. A high n_H populates the Q_1 's level $|1\rangle$ more: Q_1 becomes excited at a rate $n_H\Gamma_1$ and de-excites at a rate $(n_H + 1)\Gamma_1$. Thus, Q_1 's $|1\rangle$ level achieves its greatest population when n_H is large. When Q_1 's $|1\rangle$ is highly populated, $|101\rangle$ is highly populated. This condition is the precursor to the cooling via the cascade process $|101\rangle \rightarrow |020\rangle \rightarrow |010\rangle$.

For a different reason, low T_C values (low n_C values) favor low T_{SS} values. The levels $|020\rangle$ and $|010\rangle$ have low populations. The reverse process $|010\rangle \rightarrow |020\rangle \rightarrow |101\rangle$, which undermines the refrigeration, is therefore suppressed.

For the sake of analyzing the refrigerator's dynamics, we model with an exponential function the decay of Q_3 's excited-state population, P_{exc} , as a function of the duration Δt for which the quasithermal fields are applied (see Fig 3b). The exponential approximation appears reasonable from our measurements, particularly until P_{exc} has declined to 0.01. We denote the cooling rate of Q_3 by Γ_{cool} . Γ_{cool} is closely related to the inverse of reset time shown in Fig. 4b (the time needed for Q_3 's excited-state population to reach 0.01). In the optimization of Γ_{cool} , the dissipation rates (Γ_1 and Γ_2) and A play a critical role. Specifically, under the conditions $n_H \gg 1$ and $n_C \ll 1$, $n_H\Gamma_1$ ($= \Gamma_{1\uparrow} \approx \Gamma_{1\downarrow}$) and Γ_2 ($\approx \Gamma_{2\downarrow}$) are the relevant rates. If these rates are too small, they become the limiting factors in the cascade process $|001\rangle \rightarrow |101\rangle \rightarrow |020\rangle \rightarrow |010\rangle$ that effects the refrigeration. On the other hand, if those rates are too high, the three-body coherent-exchange process suffers excessive dephasing and becomes the limiting factor. Figure S4 shows a 2D plot of Γ_{cool}/A as a function of $n_H\Gamma_1/A$ and Γ_2/A , calculated from our 8-level population model. Optimal values of $n_H\Gamma_1/A$ and Γ_2/A maximize Γ_{cool} . Our experimental parameters fall at the gray cross-hair in Fig. S4. The maximum Γ_{cool} corresponds to a minimum in reset (the time taken to reach $P_{\text{exc}} = 0.01$). That is, Fig. S4 guides the choice of parameters used to further reduce the reset time, as illustrated in Fig. 4b of the main text. A simpler version of the model, containing only 3 levels ($|001\rangle$, $|101\rangle$, and $|020\rangle$), yields the optimal values of the parameters close to that of the 8-level model. Thus, this simpler model suffices for engineering the refrigerator. However, the 3-level model does not fit our main results quantitatively.

6. Refrigeration's dependence on cold-bath temperature

Figure S5 shows the Q_3 's excited-state population, P_{exc} , as a function of the duration Δt for which the quasithermal microwave modes are applied. We present these data at several values of the average number n_C of photons in the cold bath. The average number n_H of hot-bath thermal photons is a high value, 35.

Increasing n_C populates Q_2 's excited states incoherently, rendering the qutrit's state mixed [66]. The mixing hinders the three-body process $|101\rangle \rightarrow |020\rangle$. The refrigeration is impeded, so the steady-state P_{exc} increases.

7. Refrigeration of Q_3 initiated in its natural steady state

In this study, we begin with Q_3 in the steady state that results from Q_3 's equilibrating as much as possible with its environment. (The state may, in fact, be far from equilibrium.) According to our measurements, Q_3 's $|1\rangle$ level has a population P_{exc} of 0.028 in this state. We allow our quantum refrigerator to run for a duration Δt . Then, we perform a Rabi population measurement of $|1\rangle$. (See the pulse scheme in Fig. S4a.) P_{exc} is plotted as a function of Δt in Fig. S4. Here, P_{exc} begins at a much lesser value than in the main text's Fig. 3b. Therefore, P_{exc} reaches its long-time value, here, by an earlier time ≈ 800 ns.

We observed that P_{res} varied between 0.015 and 0.028 across long time frames (days) during the experiments. Such a large P_{res} (which is the motivation for reset) originates from uncontrolled non-equilibrium processes, such as stray infrared-radiation and inadequate device thermalization. Minute changes in the strength of these uncontrolled processes could lead to such changes in P_{res} .

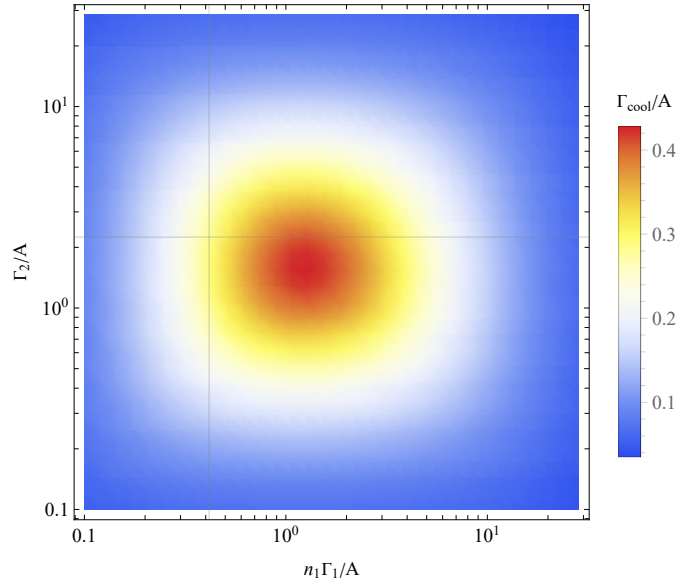


FIG. S4: Two-dimensional plot of Γ_{cool}/A as a function of $n_H \Gamma_1/A$ and Γ_2/A , calculated from our 8-level model. Γ_{cool} is defined as the rate of the decay of Q_3 's excited-state population to 0.01. The cross-hair indicates our experimentally realized values: $n_H = 19.4$, $\Gamma_1/(2\pi) = 70$ kHz, $\Gamma_2/(2\pi) = 7.2$ MHz, and $A/(2\pi) = 3.2$ MHz. The experimentally determined $\Gamma_{\text{cool}}/(2\pi) = 0.69$ MHz, which is close to the calculated $\Gamma_{\text{cool}}/(2\pi) = 0.9$ MHz.

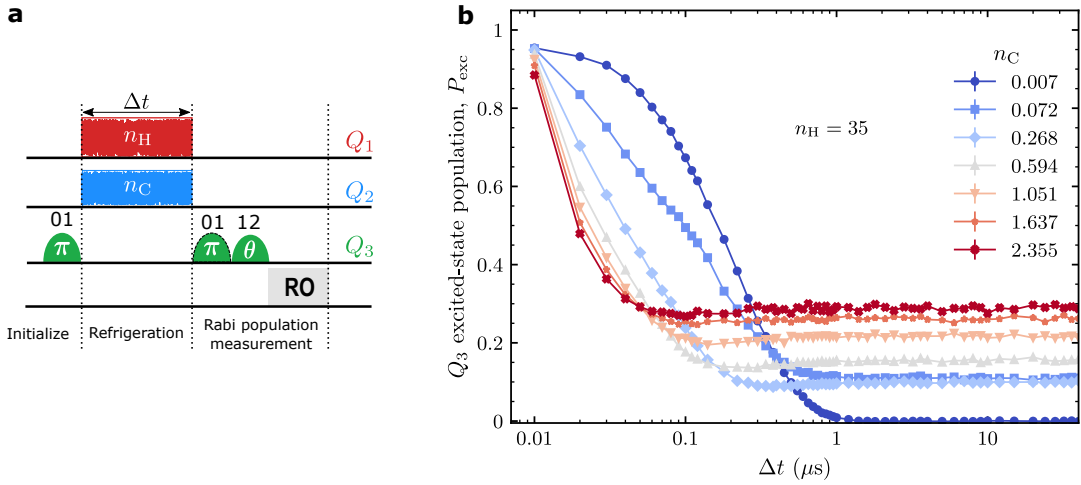


FIG. S5: Refrigeration's dependence on cold-bath temperature. (a) Pulse scheme. (b) Q_3 's excited-state population, P_{exc} , as a function of the time duration Δt of the application of quasithermal field, at select values of the average number n_C of thermal photons in the cold bath. The average number n_H of photons fixed at the high value 35.

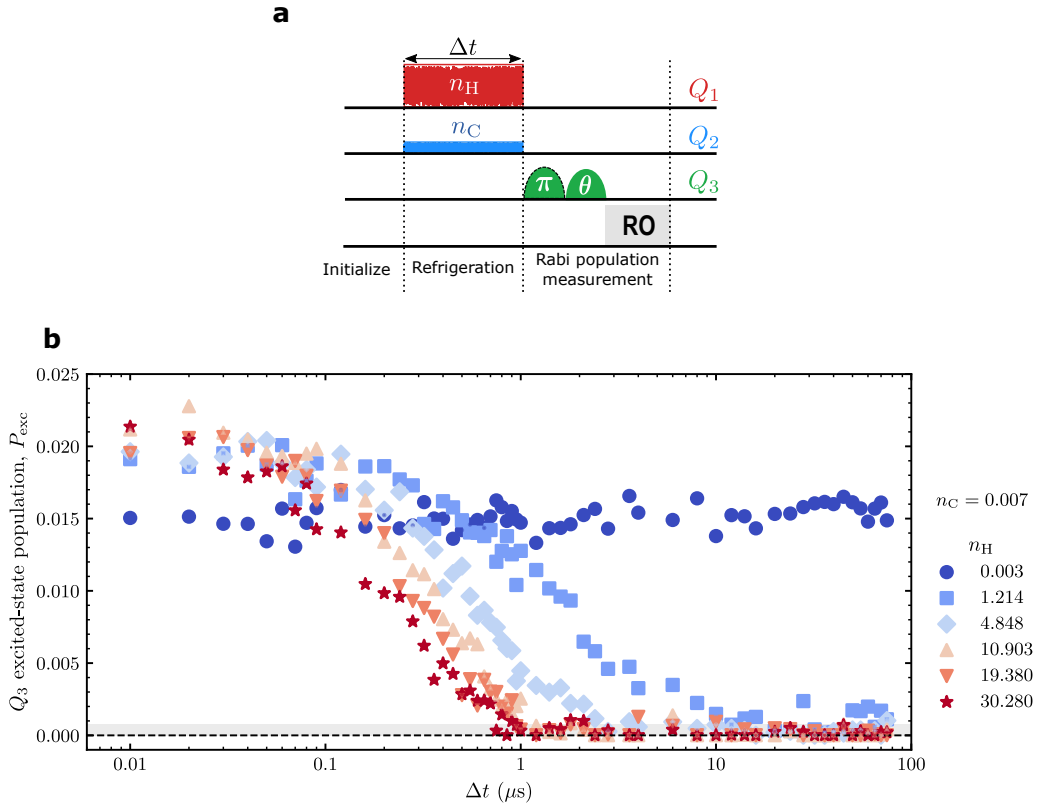


FIG. S6: Refrigeration of target qubit initialized with a residual $|1\rangle$ population of 0.020. (a) Pulse scheme. The qubit is not initialized entirely in the excited state. (b) Q_3 's excited-state population, P_{exc} , as a function of the time duration Δt of the thermal-microwave-mode pulse, for select values of the average number n_H of thermal photons in the hot bath.